



A Confinement-Driven Nucleation Mechanism of Metal Oxide Nanoparticles Obtained via Thermal Decomposition in Organic Media

Geoffrey Cotin, Benoît Heinrich, Francis Pertont, Céline Kiefer, Gregory Francius, Damien Mertz, Barbara Freis, Benoit Pichon, Jean-marc Strub, Sarah Cianférani, et al.

► To cite this version:

Geoffrey Cotin, Benoît Heinrich, Francis Pertont, Céline Kiefer, Gregory Francius, et al.. A Confinement-Driven Nucleation Mechanism of Metal Oxide Nanoparticles Obtained via Thermal Decomposition in Organic Media. *Small*, 2022, 18 (20), pp.2200414. 10.1002/smll.202200414 . hal-03663499v2

HAL Id: hal-03663499

<https://hal.science/hal-03663499v2>

Submitted on 8 Mar 2023

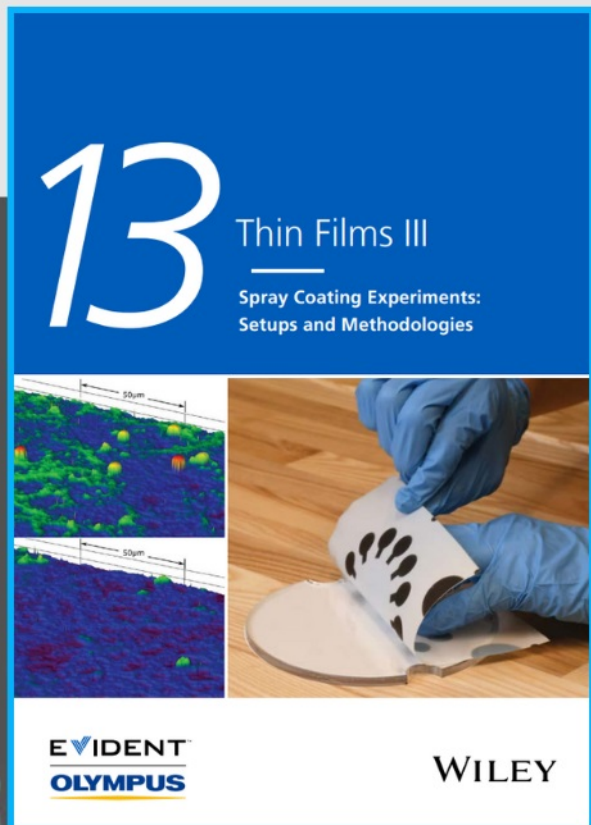
HAL is a multi-disciplinary open access archive for the deposit and dissemination of scientific research documents, whether they are published or not. The documents may come from teaching and research institutions in France or abroad, or from public or private research centers.

L'archive ouverte pluridisciplinaire **HAL**, est destinée au dépôt et à la diffusion de documents scientifiques de niveau recherche, publiés ou non, émanant des établissements d'enseignement et de recherche français ou étrangers, des laboratoires publics ou privés.



Spray Coating Experiments: Setups and Methodologies

**The latest eBook from
Advanced Optical Metrology.
Download for free.**



Spray Coating Experiments: Setups and Methodologies, is the third in our Thin Films eBook series. This publication provides an introduction to spray coating, three article digests from Wiley Online Library and the latest news about Evident's Image of the Year Award 2022.

Wiley in collaboration with Evident, are committed to bridging the gap between fundamental research and industrial applications in the field of optical metrology. We strive to do this by collecting and organizing existing information, making it more accessible and useful for researchers and practitioners alike.

EVIDENT
OLYMPUS

WILEY

A Confinement-Driven Nucleation Mechanism of Metal Oxide Nanoparticles Obtained via Thermal Decomposition in Organic Media

Geoffrey Cotin, Benoît Heinrich, Francis Pertion, Céline Kiefer, Gregory Francius, Damien Mertz, Barbara Freis, Benoit Pichon, Jean-Marc Strub, Sarah Cianférani, Nathalie Ortiz Peña, Dris Ihiawakrim, David Portehault, Ovidiu Ersen, Amir Khammari, Matthieu Picher, Florian Banhart, Clement Sanchez, and Sylvie Begin-Colin*

Thermal decomposition is a very efficient synthesis strategy to obtain nano-sized metal oxides with controlled structures and properties. For the iron oxide nanoparticle synthesis, it allows an easy tuning of the nanoparticle's size, shape, and composition, which is often explained by the LaMer theory involving a clear separation between nucleation and growth steps. Here, the events before the nucleation of iron oxide nanocrystals are investigated by combining different complementary in situ characterization techniques. These characterizations are carried out not only on powdered iron stearate precursors but also on a preheated liquid reaction mixture. They reveal a new nucleation mechanism for the thermal decomposition method: instead of a homogeneous nucleation, the nucleation occurs within vesicle-like-nanoreactors confining the reactants. The different steps are: 1) the melting and coalescence of iron stearate particles, leading to “droplet-shaped nanostructures” acting as nanoreactors; 2) the formation of a hitherto unobserved iron stearate crystalline phase within the nucleation temperature range, simultaneously with stearate chains loss and Fe(III) to Fe(II) reduction; 3) the formation of iron oxide nuclei inside the nanoreactors, which are then ejected from them. This mechanism paves the way toward a better mastering of the metal oxide nanoparticles synthesis and the control of their properties.

1. Introduction

Various iron oxide nanoparticle (IONP) synthesis methods have been set up for years, but currently one of the most adapted one allowing fine control over the structural parameters of NPs is the heated-up thermal decomposition (TD).^[1–3] Indeed, the IONPs characteristics, which need to be tuned to the targeted properties and applications (magnetism, nanomedicine, catalysis, etc.), are mainly tuned by controlling their size, shape, and composition, which is quite easy by using this TD method. The TD method developed by Hyeon et al.^[1,2,4] consists of the decomposition of an iron precursor in a high boiling point organic solvent in the presence of one surfactant, which ensures grain growth control and colloidal stability. Spherical IONPs with a controlled mean size and a narrow size distribution were thus elaborated, and different NP shapes were obtained by tuning the heating rate

G. Cotin, B. Heinrich, F. Pertion, C. Kiefer, D. Mertz, B. Freis, B. Pichon, N. Ortiz Peña, D. Ihiawakrim, O. Ersen, A. Khammari, M. Picher, F. Banhart, S. Begin-Colin
Université de Strasbourg
CNRS

Institut de Physique et Chimie des Matériaux de Strasbourg
UMR 7504, Strasbourg F-67034, France
E-mail: sylvie.begin@ipcms.unistra.fr

G. Cotin, F. Pertion, C. Kiefer, D. Mertz, B. Pichon, O. Ersen, S. Begin-Colin
Labex CSC
Fondation IcFRC/Université de Strasbourg
8 allée Gaspard Monge BP 70028, Strasbourg Cedex F-67083, France

 The ORCID identification number(s) for the author(s) of this article can be found under <https://doi.org/10.1002/smll.202200414>.

© 2022 The Authors. Small published by Wiley-VCH GmbH. This is an open access article under the terms of the Creative Commons Attribution-NonCommercial-NoDerivs License, which permits use and distribution in any medium, provided the original work is properly cited, the use is non-commercial and no modifications or adaptations are made.

G. Francius
Université de Lorraine and CNRS
LPCME UMR 7564, Nancy F-54000, France

J.-M. Strub, S. Cianférani
Université Strasbourg
CNRS
IPHC
Laboratoire de Spectrométrie de Masse BioOrganique
UMR 7178, Strasbourg F-67000, France

D. Portehault, C. Sanchez
Sorbonne Université
CNRS UMR 7574
Collège de France
LCMCP
4 place Jussieu, Paris cedex 05 75252, France

C. Sanchez
USIAS Chair of Chemistry of ultradivided matter
University of Strasbourg Institut of Advanced Study
Strasbourg 67000, France

DOI: 10.1002/smll.202200414

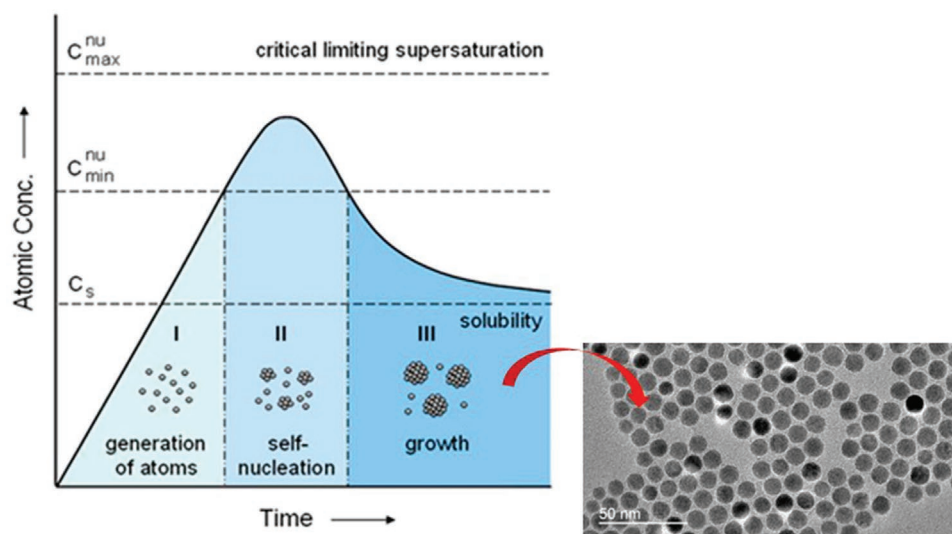


Figure 1. Variation of monomer concentration during nucleation-growth processes (right: TEM image of 10-nm-sized NPs). Reproduced with permission.^[11] Copyright 2008, John Wiley and Sons.

and using shape driving ligands, which will adsorb on specific faces of nuclei and thus promote the growth of other faces driving thus specific shapes.^[5–8] IONPs with different sizes and shapes have been thus widely synthesized using this method.

Such versatility in tuning NPs characteristics is often related to the TD process itself, which is reported to ensure a clear separation between nucleation and growth steps, which is the key factor for obtaining NPs with a narrow size distribution and also tailored specifications. Indeed, the stages between the beginning of precursor TD and the NPs formation are currently described by the nucleation and growth theory reported by LaMer and Dinegar^[9] in 1950. Three major stages are proposed (**Figure 1**): i) iron-based monomers generation (monomers are reported to result from the precursor decomposition upon increasing temperature^[4]); ii) nucleation after which a critical nucleation concentration (C_{\min}^{nu}) in the monomer is reached; iii) then the growth of nuclei after which the monomer concentration goes below C_{\min}^{nu} and stays above the saturation C_s . Therefore, nuclei are generated during the nucleation step that is followed by a homogeneous growth step without the creation of new nuclei.^[4,10,11] Such LaMer theory allows thus explaining the NPs synthesis with narrow size distribution and the possibility to obtain different shapes using shape driving ligands. The TD synthesis with its variety of experimental parameters such as temperature, reaction time, concentration, and nature of precursor, surfactants, and solvent, offers proper freedom for the design of NPs (e.g., to tune the size, morphology, and composition). However, because of these numerous parameters, there is always some lack in the IONPs synthesis control and reproducibility, which currently limit their development and make them harder to scale up, which is a prerequisite for their further use in industry.

The nucleation has been proved, by using different characterization techniques, to occur in the range of 200–300 °C and more precisely around 280 °C for iron carboxylate complexes, such as iron oleate and iron stearates.^[2,4,10,12–15] Though

research works converge on the same temperature range in which the nucleation takes place, the intrinsic TD mechanism still remains unraveled, and in particular the structure and composition of monomer generated by the decomposition of the precursor. Most interesting studies rely on ex situ analysis of samples extracted from the synthesis media at different reaction times, for example, Kwon et al.^[4] studied the TD of iron oleate in octadecene or eicosene by performing magnetic measurements, size exclusion chromatography, and transmission electron microscopy (TEM)-based analyses. They have been able to identify the temperature range of nucleation in their system, but most importantly, they reported that intermediates species, consisting of poly-oxo iron complexes named monomers, are formed before the nucleation step. More recently, Lassenberger et al.^[16] studied the in situ NPs formation with small angle X-ray scattering (SAXS). They have decomposed iron pentacarbonyl ($\text{Fe}(\text{CO})_5$) with oleic acid (OA) in dioctylether (OE) and were able to show that the synthesis mechanism takes place in several stages. First, an iron oleate is formed from the reaction of the precursor with OA, then structures that are not crystallized NPs are observed before the burst of nucleation and then the growth step. These structures were ascribed to the polyiron oxo species reported by Kwon et al.^[4] but they suggested that it could be micellar structure of OA encapsulated precursor. In fact, the stages before nucleation are quite complex to analyze using standard characterization techniques.

In that challenging context, with the aim to get a better insight into the TD mechanism, we investigated the early and different stages up to the nucleation step of the TD process by combining different in situ characterization techniques. The iron precursor is an iron stearate with a composition 1Fe:2St (one iron atom for two stearate (St) chains named FeSt_2) synthesized “in-house” by coprecipitation in water.^[12,13,17] The composition and structure of this iron stearate, FeSt_2 , were studied, and it consists of a lamellar compound composed

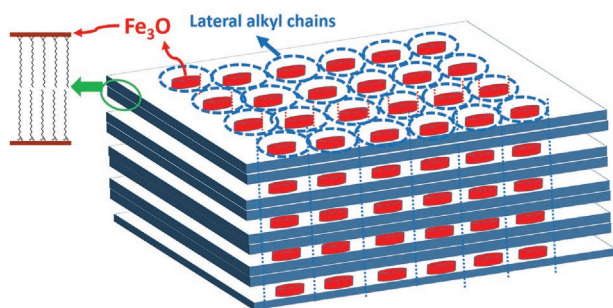


Figure 2. Schematic structure of FeSt_2 : planes with a hexagonal arrangement of polynuclear iron complexes separated by double layers of all-trans stearate chains perpendicular to polynuclear complex planes.

mainly of the polynuclear complex $[\text{Fe}_3(\mu_3\text{-O})\text{St}_6\cdot x\text{H}_2\text{O}]\text{Cl}$.^[17] The iron polycations are organized in planes separated by perpendicular stearate chains in an all-trans configuration (Figure 2). The reproducible synthesis of 10 nm-sized NPs has been demonstrated with this precursor.^[12] Recent investigations confirmed the reported hypotheses that the nuclei, in such reaction media with iron carboxylate precursor, display a wüstite composition.^[13] They also suggested a nucleation mechanism based on the condensation of these polynuclear complexes after their catalytic decarboxylation occurs simultaneously with the reduction of Fe(III) in Fe(II) .^[13,17,18] In this present work, we investigated the stages leading to nuclei formation. We have considered FeSt_2 and also heat-treated FeSt_2 (at 140 °C for 48 h), named FeSt_{2d} because they led to the same NPs size in the standard 10 nm NPs synthesis conditions (Figure S1, Supporting Information). Worthy to note that FeSt_{2d} showed a slightly faster reaction, and NPs with anisotropic shapes were easier to obtain.^[6,12] In fact, in contrast with FeSt_2 , FeSt_{2d} is composed of a mixture of $[\text{Fe}_3(\mu_3\text{-O})\text{St}_6\cdot x\text{H}_2\text{O}]\text{St}$ and $[\text{Fe}_7(\mu_3\text{-O(H)})_6(\mu_2\text{-O(H)})_x\text{St}_{12-x}]\text{St}$ polynuclear complexes (details in Figures S2–S4, Supporting Information).

The TD mechanism of these iron stearates up to the nucleation step has been analyzed in depth by combining several fine and powerful characterization techniques such as liquid-phase TEM, in situ TEM at high temperature, atomic force microscopy (AFM) in an organic liquid, small and wide-angle X-ray scattering (SWAXS) of powdered samples, and SAXS of reaction solutions. SAXS and SWAXS techniques were used because metal stearates are long-chain carboxylate compounds, which are well known to exhibit a liquid crystal (LC) behavior,^[19–23] and the effect of this behavior needs to be studied. Thermogravimetric analyses (TGA) on iron precursors were shown very suitable to establish the temperature ranges of the nucleation and growth steps, and thus, TEM at high temperature on iron stearate powders provided useful information on the evolution of iron stearate particles up to the nucleation step. Liquid-cell TEM (LCTEM)^[24–28] has already been used in the fields of electrocatalysis^[29] and energy storage as well as for investigating biological cells^[24] and nanomaterials synthesis.^[30–32] However, one may notice that studies on NPs synthesis mechanisms deal mainly with the growth process of metallic or bimetallic or core-shell NPs (Cu, Pd, Pt, Au, Au-Pd, Fe_3Pt ...).^[33] With iron oxide NPs in particular, the colloidal stability of iron oxide NPs, their aggregation mechanisms

leading to nanorods, or the growth step of iron oxide NPs, have been reported, but nothing on the type of monomers and on the stages before the formation of nuclei to the best of our knowledge.^[25,32,34–37] It is often reported that there is no temperature increase during LCTEM and rather radiolysis reactions involving mostly water. The radiolysis of water generates radicals inducing reducing or oxidizing reactions in the liquid phase.^[25,38,39] The electron beam was also reported to favor the reduction of ions. In our specific case, LCTEM is thus expected to favor the reduction of Fe^{3+} bound to carboxylate groups: it would thus simulate suitably the effect of the temperature on the precursor decomposition: a reduction of Fe^{3+} in Fe^{2+} simultaneously with the departure of two stearate chains which decompose into ketone, water, and CO_2 (which is observed thermally in the nucleation temperature range [200–300 °C]). Indeed, a decarboxylation catalyzed by iron(III) cations, leading to a reduction of iron(+III) to iron(+II), has already been reported.^[18] Therefore, LCTEM, performed on preheated reaction mixtures, provided useful information on the nucleation mechanism.

In addition, most LCTEM experiments have been conducted in water, and there are only very few experiments in organic solvents.^[39–41] However, even in organic media, these experiments reported always the presence of a small amount of water, inducing the presence of radicals to explain the observed reactions. In our case, we use a reaction media, preheated at a temperature lower than those reported for the nucleation step but which has already begun to react/evolve. Thus, such a study, quite without water due to the preheating step at 120 °C, will shed light on the potential of such a technique for mechanistic investigations in organic solvents.

The different stages occurring up to the nucleation step have been analyzed by combining these different characterization techniques. We evidenced thus, for the first time, that the nucleation, either in the powder state or in the liquid reaction media, occurs inside nanoreactors with the vesicle/droplet aspect in which the reactants are confined.

2. Results

During the 10 nm NPs standard synthesis, the mixture is stirred and heated at 120 °C for 1 h without a reflux condenser to dissolve the reactants and remove the volatile molecule residues; afterward, the reaction mixture is heated up to about 290 °C at 5 °C min^{-1} and maintained for 2 h at this temperature. IONPs with a mean diameter of 10 nm are thus reproducibly obtained (Figure S1, Supporting Information). From earlier published results^[2,4,14,16] confirmed by investigations on these iron stearates,^[12] the nucleation of iron oxide NPs occurs in the range of 200–300 °C with the observation of stable nuclei from around 280 °C. In this whole temperature range of 200–300 °C (Figure S5, Supporting Information),^[12] a high weight loss is also noticed related to the vanishing of carboxylate chains^[13] and more precisely, to the loss of two stearates for FeSt_2 , whose composition is $[\text{Fe}_3(\mu_3\text{-O})\text{St}_6\cdot x\text{H}_2\text{O}]\text{Cl}$.^[17] We have thus investigated the thermal behavior of iron stearate powders before and after 200 °C and performed LCTEM on the reaction mixture after the preheating treatment at 120 °C.

2.1. Thermal Transformation Steps of the Iron Stearate Powders up to 200 °C

2.1.1. DSC and SWAXS Experiments on Iron Stearate Powders Before the Beginning of the Nucleation Step (Below 200 °C)

SWAXS and differential scanning calorimetry (DSC) analyses provided complementary information on the structural evolution of the iron stearate precursors with temperature (Figures S6 and S7, Supporting Information). These analyses are described in Supporting Information. FeSt_2 , with the main composition $[\text{Fe}_3(\mu_3\text{-O})\text{St}_6\text{xH}_2\text{O}]\text{Cl}$, displays a lamellar rotator (Lam) structure consisting of alternating ionic layers and double-layers of alkyl chains crystallized in a 2D hexagonal rotator lattice (Figure 2).^[42,43] FeSt_{2d} is on the contrary an amorphous solid composed of a mixture of $[\text{Fe}_3(\mu_3\text{-O})\text{St}_6\text{xH}_2\text{O}]\text{St}$ and polynuclear complexes (polycations) with higher Fe content (formula $[\text{Fe}_7(\mu_3\text{-O}(\text{H}))_6(\mu_2\text{-O}(\text{H}))_x\text{St}_{12-x}]\text{St}$) in agreement with the characterizations described in Supporting Information. In fact, several species are certainly formed during the prolonged annealing of FeSt_2 at 140 °C leading to FeSt_{2d} , and the associated 12% weight loss reduced the stoichiometry in stearate in an inhomogeneous way. The presence of polynuclear complexes with higher Fe content and lower Fe/St ratio is in agreement with such observation of stearate chain elimination. Nevertheless, a brief fluidification at 120 °C led to its reorgani-

zation into a hexagonal columnar LC, and a Lam structure was recovered on subsequent cooling (Figure S6, Supporting Information). A hexagonal columnar LC was also formed for FeSt_2 above its melting temperature lying around 100 °C. Expectedly, both compounds showed different transition temperatures to isotropic liquid (140 °C for FeSt_2 and 175 °C for FeSt_{2d}) since their stoichiometries are different (Figure S8, Supporting Information). All these DSC and SWAXS experiments show that after a heat-treatment to 120 °C of both stearates and cooling down to room temperature (RT), the lamellar structure is recovered. They also confirm that the crystalline phases are entirely vanished after the heat-treatment step at 120 °C to homogenize the reaction mixture during the NPs synthesis process.

2.1.2. TEM Experiments under Vacuum below 200 °C

TEM experiments at different temperatures were performed on FeSt_2 powder deposited on an amorphous carbon film of a TEM grid (Figure 3). The flakes of the lamellar compound are visible in the TEM image taken at RT. Heating the powder in a TEM heating stage leads to the morphological transformations shown in Figure 3. Slightly above 100 °C, the compounds start melting and form droplet-like structures. A coalescence of these droplets is also observed and explains the observation of different droplet sizes. Below 200 °C, the SAED patterns

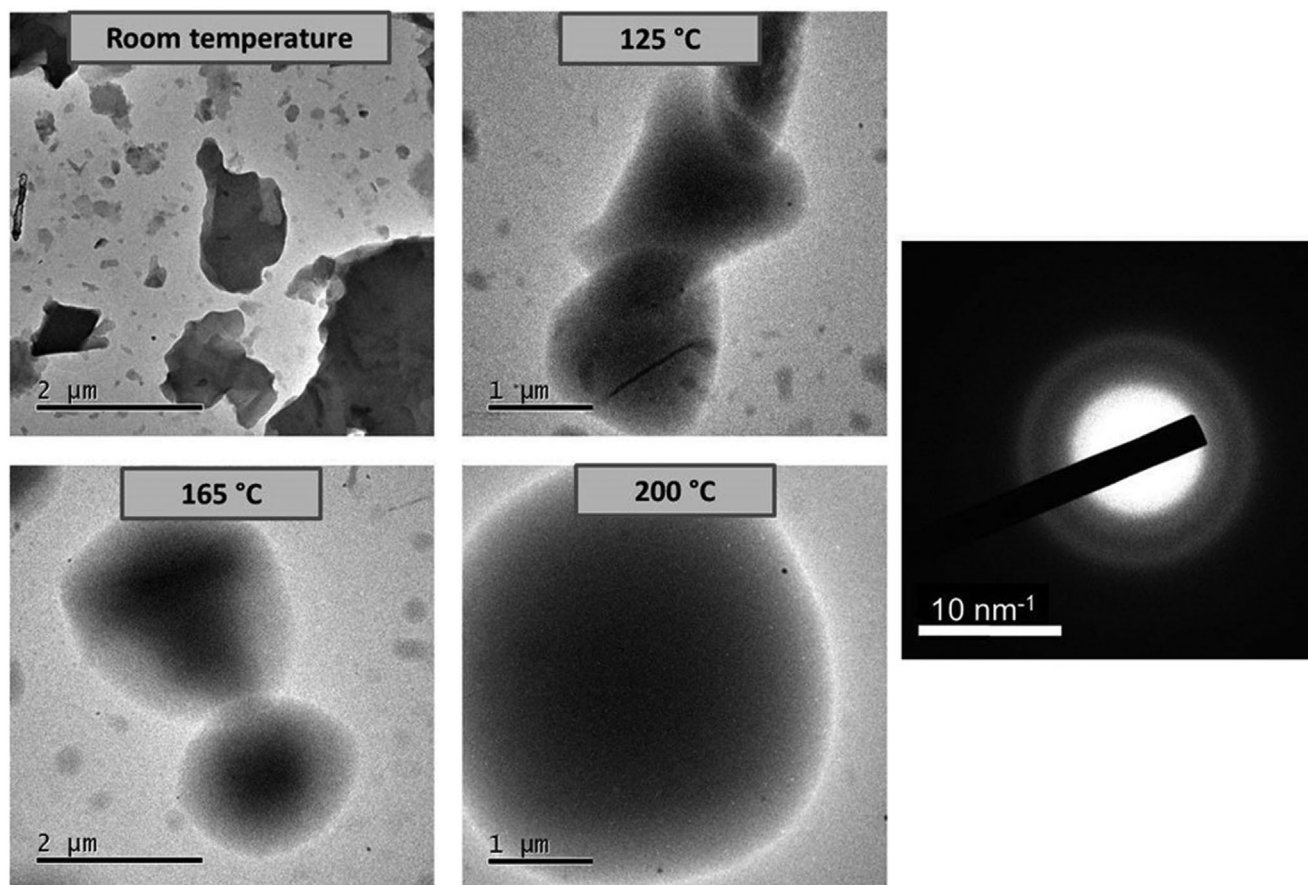


Figure 3. TEM images taken from powders of FeSt_2 (left) as a function of temperature and SAED pattern at 200 °C (right).

(Figure 3) show that these droplet-like particles are amorphous in agreement with previous DSC and SWAXS experiments. After cooling, amorphous solid objects with a globular morphology remain.

To get information about the speed of such transformations, short heat pulses can be applied instead of continuously heating the specimens. This has been done by sending infrared nanosecond laser pulses onto the compounds in the TEM and observing their transformation. Under laser pulses of moderate intensity (1064 nm, 7 ns), the same morphological transformation of the powder as under continuous heating is observed (Figure S9, Supporting Information). After one pulse (25 μ J on a specimen area of 150 μ m in diameter), the effect of melting and coalescence is already obvious. Since the specimen is heated within 7 ns (duration of the IR pulse) and cools down within some tens of microseconds, the structural transformations are very fast. The delay between the IR pulses was several seconds to minutes so that the specimen was always at RT when the images were taken. Repeated IR pulses lead to ongoing coalescence of the vesicles.

Thus, continuous heating of FeSt₂ particles (Figure 3 and Figure S9, Supporting Information) leads first to the melting and transformation of the flake-like structure of iron stearate particles into spherical droplet-like particles. Up to 200 °C, the particles remain amorphous and tend to coalesce.

2.2. TEM Experiments under Vacuum in the Temperature Range 200–280 °C

Figure 4 and Figure S10, Supporting Information, show the evolution of the iron stearate particles under static heating in a vacuum at temperatures above 200 °C. Above 220 °C, the droplet-like particles appear to be surrounded by another phase (shell with lower contrast, Figure 4b,c and Figure S10, Supporting Information). This shell of 200–300 nm thickness shows less electron scattering due either to the absence of heavier elements such as Fe (which should prevail in the darker core) or due to the absence of a crystalline phase that diffracts the beam (the images were taken under multi-beam conditions). This shows that separation into two phases occurred above 200 °C. The weak contrast of the shell, despite its considerable thickness, indicates an organic (hydrocarbon) material that does not contain considerable amounts of iron.

Above 200 °C, a crystallization of the droplet-like particles is observed (Figure 4) and occurred quite simultaneously with the appearance of the white shell around the droplets. The crystalline phase remains stable upon further heating up to 270 °C. Above 220 °C, the particles seem fully crystallized without a visible loss of volume with respect to the droplet-like particles below 175 °C. In many particles, diffraction contours along a crystal defect are visible as dark lines (Figure 4c–e and

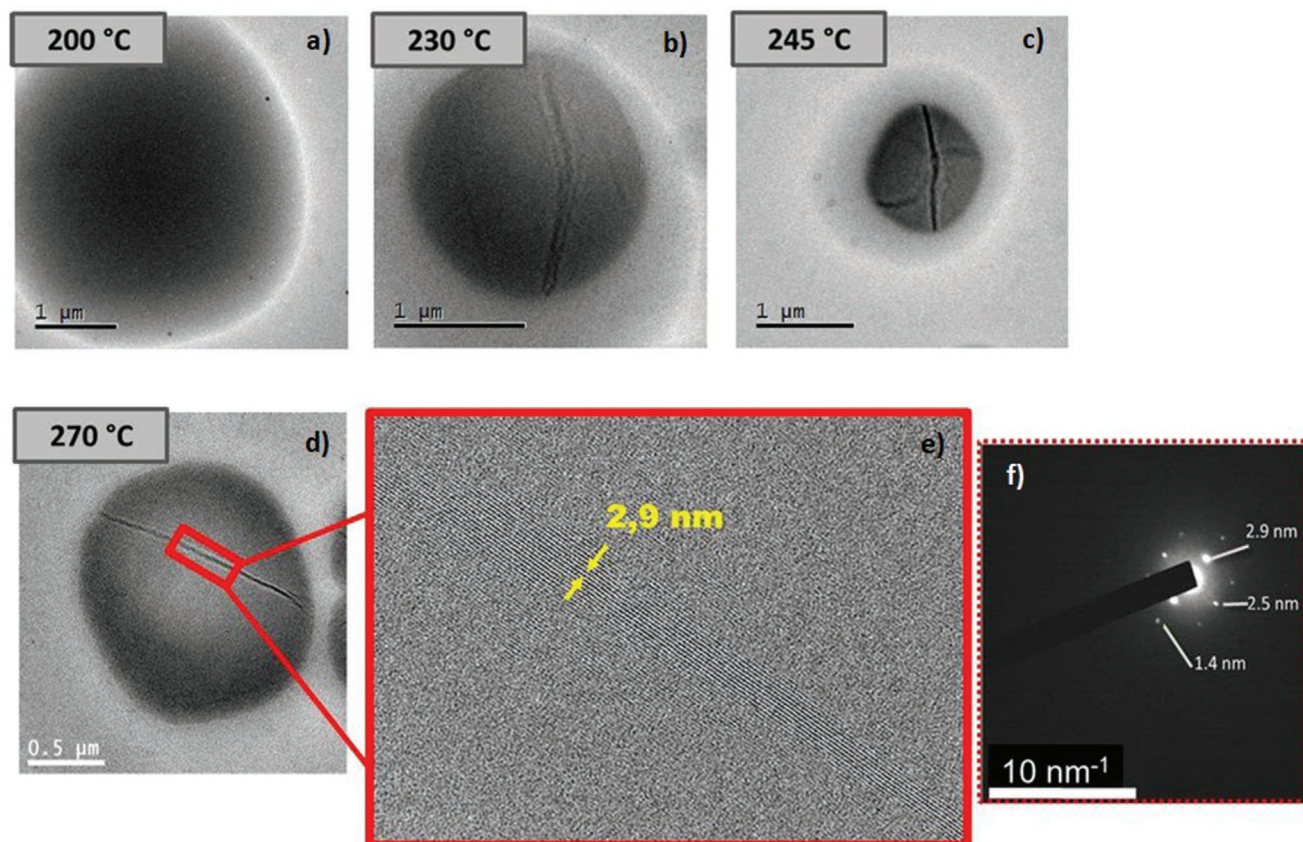


Figure 4. TEM images of FeSt₂ powders in the temperature range 200–280 °C (a–d). In the low-magnification images (b–d), the dark lines correspond to planar defects in a crystalline structure. At high resolution, the lattice of the crystalline Fe₂St phase is getting visible. e) An HRTEM image including the defect in (d). The diffraction pattern (f) shows the corresponding reflections. The amorphous shell around the droplets is visible in (b) and (c).

Figure S11, Supporting Information). These defects could be grain boundaries separating different crystal orientations or cracks resulting from thermal chock (Figure 4e). Subsequent cooling of the system showed that these transformations are irreversible, and the crystalline structure persists upon cooling to RT. The largest interplanar spacings are 2.9 and 3.2 nm. They appear to be characteristic of a molecular crystal, and they are much larger than typical lattice spacings of oxides. On the other hand, the observed spacings are lower than the interlamellar distances measured in FeSt_2 ($d(001) = 4.95 \text{ nm} \approx 2L$ (L = length of a stearate chain) and indicate a partial interdigitation of stearate chains or the presence of an angle between the iron layer and the alkyl chains as described in Figure S12, Supporting Information. Indeed, upon heating, there is a melting of stearate chains (cf. Figure S6, Supporting Information), which affects the interlamellar distances and their local organization. In addition, we know that there is also a loss of two stearate chains in the range of 200–300 °C, and the crystallization occurs quite simultaneously with the formation of the white shell around droplets. We suggest thus that the observed crystallization occurs simultaneously with the loss of stearate chains. Such a loss would induce a re-organization of iron stearates leading to a crystalline phase. One may notice that in this temperature range, the beginning of condensation between Fe_3O units in Fe_3OSt_6 complexes has been reported previously.^[2,44–46]

2.3. TEM Experiments in Vacuum above 280 °C

Above 280 °C, the transformation of the molecular crystal to iron oxide nuclei is observed (Figure 5 and Figure S13, Supporting Information). The average sizes of the oxide crystals are $\approx 5\text{--}10 \text{ nm}$ at 300 °C. The diffraction pattern allows identifying the FeO (wüstite) phase (Figure 5). This is in agreement with previously published results which have already demonstrated that the nuclei appear in the wüstite phase.^[13]

2.3.1. Fast Heating with Nanosecond IR Pulses

Besides static heating, the direct transformation of iron stearates to oxide NPs is also possible by heating with short IR laser pulses. Several IR pulses with moderate intensity (to avoid evaporation) were applied. A complete transformation from stearate flakes to oxide crystals needs several pulses (in spans of several seconds between the pulses), but the crystalline intermediate phase did not appear. These experiments, which are described in Supporting Information (§ fast heating by using laser pulse, Figures S14–S17, Supporting Information), allow concluding that the transformation of iron stearates to oxide nanocrystallites occurs at the microsecond timescale if the temperature during the laser pulses is high enough. Since the formation of the crystalline molecular phase does not occur under laser pulses, we can conclude that the crystallization of the stearate phase is slow and only appears under close-to-equilibrium conditions. Furthermore, this phase does not seem to be a necessary step in the nucleation of oxides.

These high-temperature TEM results are in agreement with earlier results, which reported the nucleation of oxide crystals at around 280 °C. They strongly suggest that the nucleation occurs in confined systems (droplet-like nanostructures which can be assimilated as nanoreactors), which originate from the melting of stearate particles.

2.4. Study of Liquid Reaction Media in Organic Solvent Pre-Treated at 120 °C

After these investigations on powders, further characterizations have been performed on reaction media solutions, consisting of a liquid mixture of iron stearate, oleic acid in dioctylether solvent, which has been submitted to a homogenization treatment at 120 °C for 60 min. Such reaction mixture leads during the TD process up to 290 °C to IONPs with a mean size of 10 nm (Figure S1, Supporting Information).

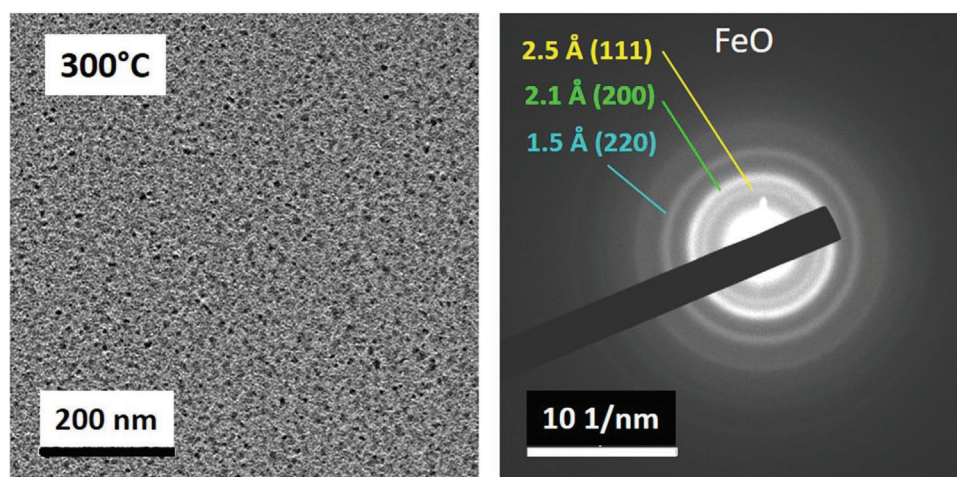


Figure 5. Characteristic TEM image at 300 °C showing the nucleation of iron oxide nanocrystals (left). The diffraction pattern (right) shows the diffraction rings of FeO.

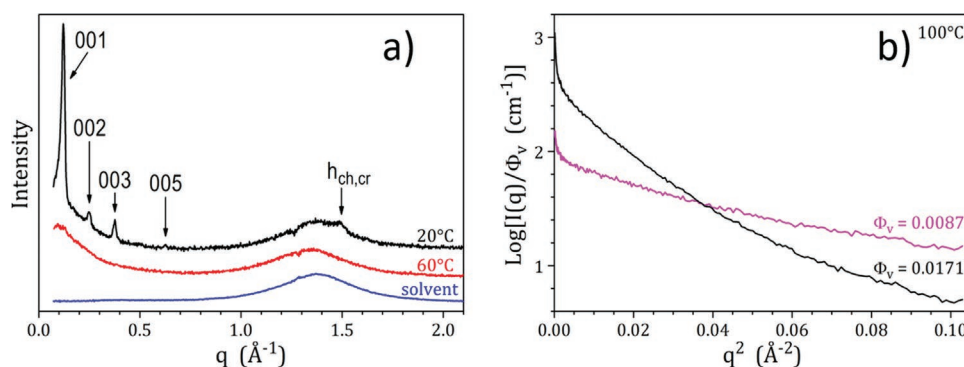


Figure 6. a) SWAXS patterns of standard 10 nm NPs reaction mixture at 20 and 60 °C using FeSt₂ (FeSt_{2d} in Figure S18, Supporting Information), as compared to solvent (dioctylether). b) Guinier representation of SAXS data for two volume fractions of FeSt₂ in dioctylether and in presence of two equivalents of oleic acid. Scattering curves were recorded at 100 °C, subtracted from solvent and renormalized.

2.4.1. SWAXS Characterization

After such a “solubilization” step of reactants at 120 °C, the resulting cooled mixture solutions were analyzed by SWAXS (Figure 6a and Figure S18, Supporting Information). SWAXS patterns show that they form suspensions of the same lamellar rotator phase as powder systems (Figure 6a and Figure S6, Supporting Information). Such liquid mixtures pass the Krafft temperature around 40 °C. At 60 °C, a clear solution is obtained and all reflections vanish, leaving only the broad scattering signal at 1.4 \AA^{-1} from solvent molecules interactions. Nevertheless, a scattering upturn is clearly visible at small angles, which indicates the presence of aggregates in the solution. To specify the aggregation nature, two diluted solutions of FeSt₂ (volume fractions $\Phi_v = 0.0087$ and 0.0171) in dioctylether and in presence of two equivalents of oleic acid were recorded in SAXS at low angles, subtracted from solvent and renormalized (Figure 6b). The low-angle scattering signal clearly confirms that aggregates subsist in solution at 100 °C, thus far from the Krafft temperature. However, the scattering profiles are different for both concentrations, revealing that there are no aggregates of defined size and isolated in the solution. At the highest concentration, the steeper decrease of the scattering should indicate a larger average aggregate size. A quantitative analysis is not possible given the profile shape variation between concentrations.

2.4.2. DLS Measurements

The presence of “nanostructures” in the reaction media upon heating up of the system was further confirmed with DLS measurements as a function of temperature (Figure S19, Supporting Information). At low temperatures, “structures” with hydrodynamic diameter in the micrometer size range are observed in particle size distribution measurements. When the temperature becomes higher than the melting temperature of FeSt₂ (60 °C), a clear decrease in the mean hydrodynamic size is noticed (Figure S19, Supporting Information). Therefore, these DLS measurements suggest strongly the presence of nanostructures in the heated reaction media whose size decreases when the temperature increases.

2.4.3. Liquid AFM Technique

Preheated reaction media was deposited just after the heating step on a functionalized substrate for observation with an original liquid AFM technique in an organic solvent. Liquid AFM images are given in Figure 7a and Figure S20, Supporting Information, and revealed a homogeneous distribution of nanostructures over the whole surfaces just after deposition on the substrates. From the AFM images, at least two populations with different sizes can be measured. Interestingly, the size distributions are quite monomodal. FeSt₂ presents a major population around $53 \pm 6 \text{ nm}$ and a second one around $74 \pm 7 \text{ nm}$ when the heat-treated precursor FeSt_{2d} presents two populations equivalent in presence at around 37 ± 6 and $175 \pm 4 \text{ nm}$.

Those nanostructures are observed to spontaneously assemble to form “rings,” as seen for FeSt₂ in Figure 7a. Indeed, we observed an aging effect. If AFM is not performed just after the heating step but after cooling down the reaction mixture and some aging time, a coalescence of the nanostructures is observed leading to nanostructures with submicronic–micronic sizes (Figure 7b,c). This would explain DLS measurements with a decrease of the nanostructure size when the temperature increases, as well as SWAXS experiments at different concentrations. In liquid, the size of these nanostructures would decrease with the temperature increases, and when the temperature decreases, they coalesce into bigger nanostructures.

AFM profiles on these submicronic nanostructures (Figure 7d and Figure S21, Supporting Information) suggest that they consist of stacked layers/sheets. The measured lamellar distance is in agreement with that of the pristine iron stearate ($d(001) = 49.5 \text{ \AA} \approx 2L$ [L = length of a stearate chain]) confirming again that, under cooling, the lamellar structure is recovered.

2.4.4. CryoTEM

CryoTEM allowed investigation of a thin vitrified film of the reaction media solution in which all processes are stopped by plunge-freezing in an appropriate coolant.^[26] The organization/structuration of nanostructures in assemblies of nanosheets or stacked sheets has also been evidenced by cryoTEM performed

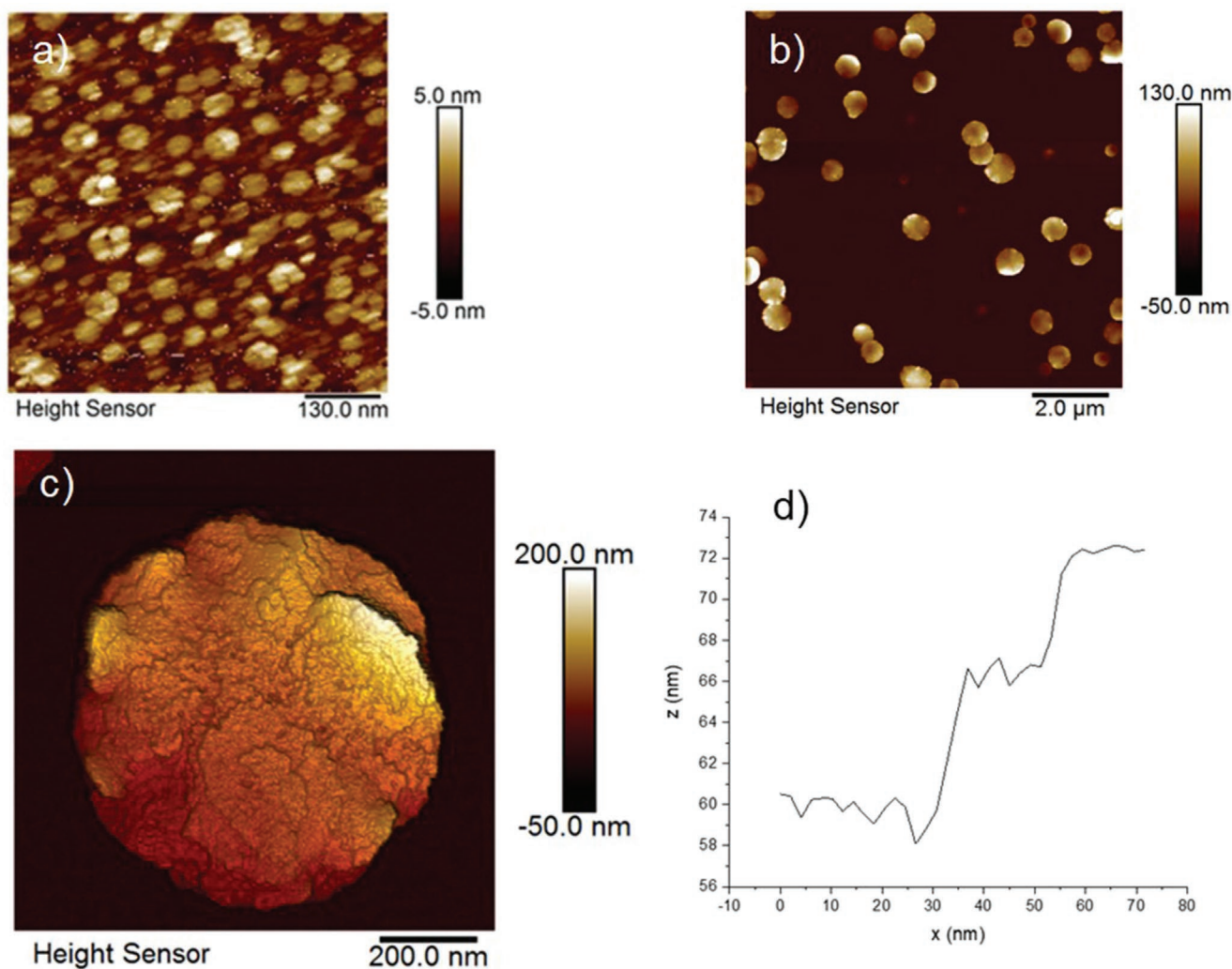


Figure 7. Liquid AFM just after deposition on a functionalized substrate of the “just prepared” pre-heated mixture (reaction mixture with FeSt_2) (a) and after ageing (b). High magnification of “aged” nanostructures (c) and AFM profile of an “aged” nanostructure (d) from (c).

on the FeSt_{2d} reaction mixture (Figure 8). The presence of iron in these nanostructures has been confirmed by EDS analysis and also by classical EDX elemental mapping during TEM analysis in the vacuum detailed in Figure S22, Supporting Information.

2.4.5. LCTEM Study of Reaction Mixture Preheated at 120 °C in an Organic Solvent

A reaction mixture involving all the reactants for the synthesis of the standard 10 nm spheres with $\text{FeSt}_{2,d}$ was imaged by TEM in the liquid cell in organic media just after the homogenization step at 120 °C for 60 min. The in situ cell TEM image is given in Figure 9 and evidences the presence of spherical structures. Indeed, after a given time of irradiation with the electron beam, FeSt_{2d} reaction mixtures present two populations of spherical structures (Figure 9). The first population presented a sharp dark/grey contrast homogeneous within the structure with a mean size centered on 15 nm. The second population is

characterized by a lighter intensity. The size of this last structure is in the range of 30–50 nm, and its characteristics are typical of droplets. Note that the dioctylether solvent was imaged alone, and no bubbles/droplets were observed in this case under the same irradiation conditions. Considering the atom mass and the composition of the reaction mixture, the dark/grey droplet-shaped nanostructures are expected to contain iron. This additional analysis confirms the hypothesis that such nanostructures originate from the reaction mixture. The observation of such nanosized structures is in agreement with the previous results demonstrating the presence of nanostructures in preheated reaction media.

LCTEM images (Figure 9) as a function of the irradiation time of the reaction mixture showed further that both white and grey nanostructures are preserved and that the nucleation occurs only in dark nanostructures. Indeed, dark points appear in the grey nanostructures when the irradiation time increases and are in particular visible in Figure 9h. These observations were similar to those during TEM experiments in temperature support that the nucleation occurs in confined media. Iron

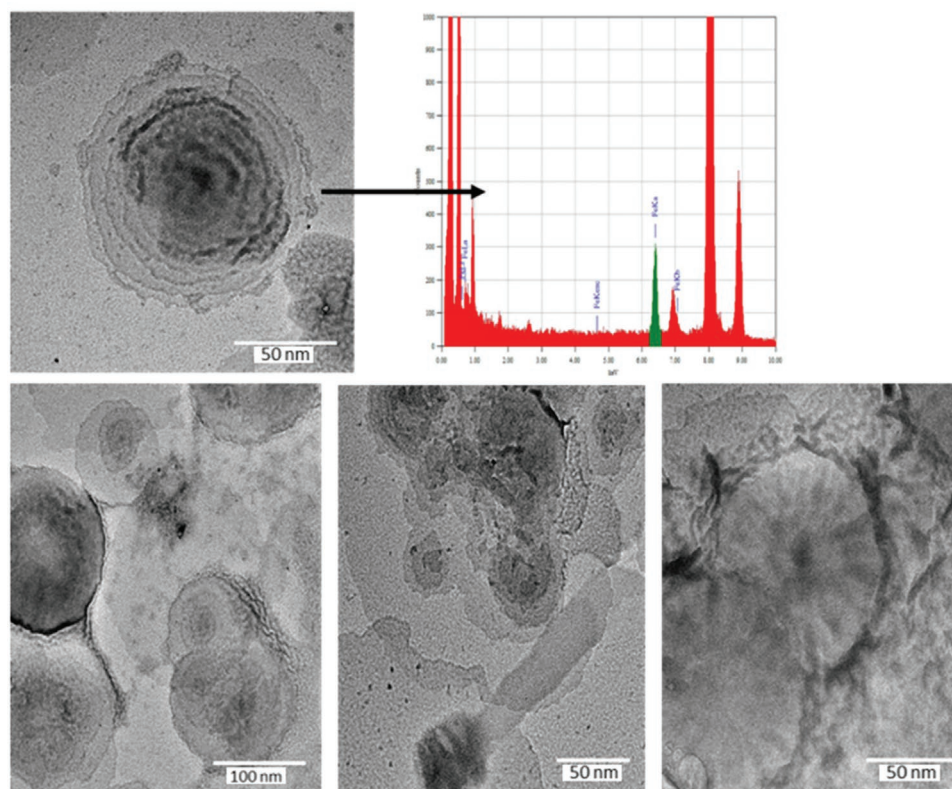


Figure 8. CryoTEM images after freezing of reaction media with FeSt_{2d} and EDS spectra showing the presence of iron (green peak) in these nanostructures.

oxide NPs have been observed at the end of both experiments conducted with only the iron stearate powder (Figure 5) or the reaction media (Figure S23, Supporting Information). The iron

oxide nuclei obtained during TEM experiments have a wüstite composition, which is in agreement with previous results^[13] when their composition is that of the spinel iron oxide during

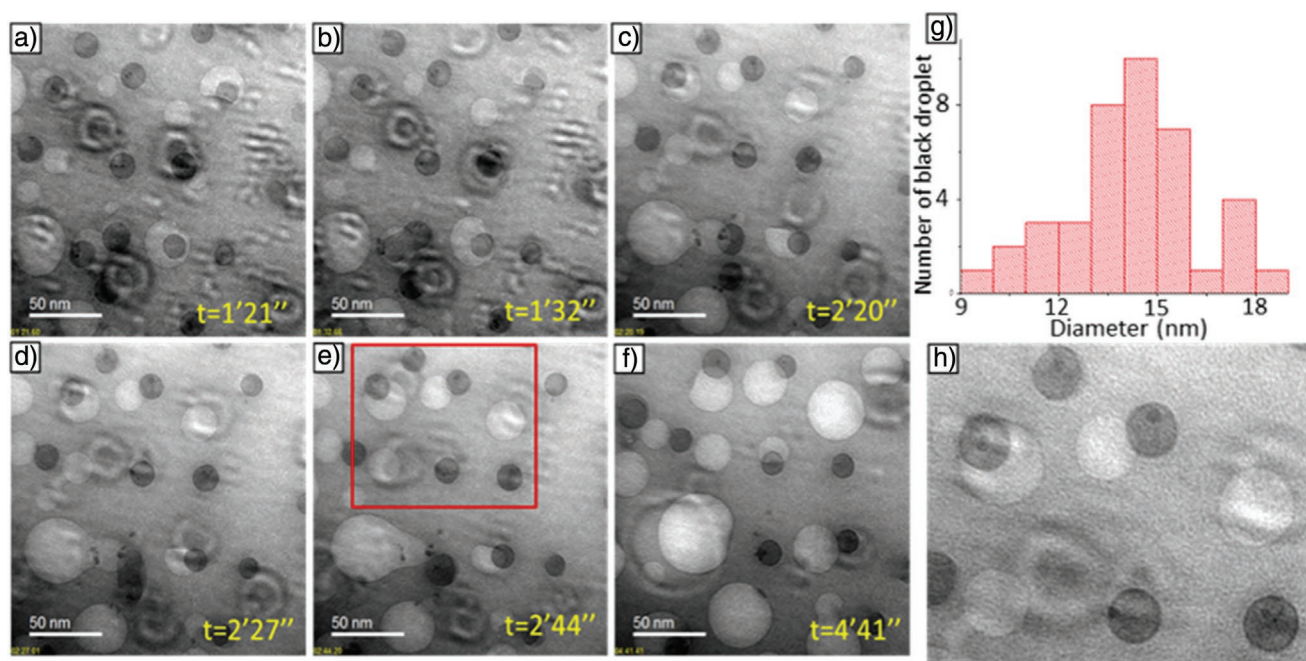


Figure 9. In situ liquid cell TEM experiments of some representative areas from reaction medium with FeSt_{2d} after different exposure times to the electron beam (a–f) and histogram of the size distribution of the contrasted structures (g) and the zoom of the red rectangle area from (e) in (h).

LCTEM experiments (Figure S23, Supporting Information). The measured lattice spacing values given in Figure S23, Supporting Information: (220) (0.287 nm) and (022) 0.242 nm, are very close to those of the iron oxide spinel structure. Indeed, the nuclei were in contact with air during these spacing measurements, and it is well known that Fe^{2+} is very sensitive to oxidation at the nanoscale.^[13,10]

Concerning the white nanostructures, there are several hypotheses: one hypothesis could be that they consist of vesicles stabilized by a double layer of oleic acid. Indeed the amount of oleic acid added is very high and should favor the reversed vesicle formation.^[47–49] However, their “inner” intensity is very different from that of outside liquid, and thus they cannot be assigned to such reverse vesicles. Such “white” bubbles have also been observed during LCTEM in presence of water and attributed to radiolysis of water leading to H_2 bubbles.^[50] However, in our case, we are in the organic solvent, and the mixture has been preheated to 120 °C; thus the presence of water should be scarce. Considering the high amount of white bubbles and the reaction conditions, such white nanostructures should not be due to the radiolysis of water. In fact, the observations that i) the formation of iron oxide nuclei is observed under electron beam irradiation and ii) that the nucleation mechanism is induced by condensation of iron stearate radicals resulting from a reduction of Fe^{3+} in Fe^{2+} in iron stearate polycations simultaneously with the departure of two stearate chains which decompose into ketone, water, and CO_2 , led us to make the hypothesis that the white bubbles could consist of CO_2 bubbles. However, water is also generated by the decomposition of stearate chains and thus radiolysis of water is not excluded. In addition, even if very few LCTEM studies have dealt with organic solvents, it has also been reported that a gaseous radiolysis product of ethanol would be H_2 ^[39,41] and the radiolysis of ethers^[51] leads to H_2 formation. Hydrocarbons have been reported as radiolytic products of fatty acids.^[52] Therefore, H_2 bubbles are not completely excluded.

By analyzing the recorded videos as a function of irradiation time (cf. one characteristic video in Supporting Information), we noticed that in some dark nanostructures, some black nuclei formed but then redissolved (cf. enclosed video and inside yellow circles in **Figure 10**). By contrast, when nuclei seem to be enough stable, they are ejected outside the black nanostructures (inside red circles in **Figure 10**). This phenomenon is observed several times in video. Some nanostructures are observed to merge (**Figure 10**, green circles), and then some nuclei are formed and ejected. Such observations confirm the LaMer mechanism but evidence also that the nucleation occurs in confined droplet-like nanostructures acting as nanoreactors. Such a mechanism explains why there is a very efficient and clear separation of nucleation and growth steps.

3. Discussion

The general physicochemical steps observed from the iron stearate precursors (FeSt_2 , FeSt_{2d}), either in the powdered state (**Figure 11**) or in the reaction mixture (**Figure 12**), to the IONPs formation have been summarized in the simplified cartoons presented in **Figures 11 and 12**.

DSC and SWAXS experiments on powders demonstrated that, after heating up to 120 °C (the homogenization temperature of the reaction mixture) and cooling down, both steirates recovered the lamellar structure and that when heating above 140 °C (FeSt_2) or 175 °C (FeSt_{2d}), an isotropic medium is obtained. TEM on powders at high temperature showed that iron stearate particles melt and form droplet-like particles (**Figure 11**), which can merge when the temperature increases and are amorphous below 200 °C (in agreement with DSC and SWAXS experiments). The characterizations done on the reaction mixture (heat-treated at 120 °C) by SAXS, liquid cell TEM, and AFM evidenced the presence of very small droplet-shaped nanostructures with two size distributions (**Figure 12**). Liquid AFM and cryoTEM demonstrated that nanostructures obtained from a reaction mixture heat-treated at 120 °C and cooled down consist of stacked planes/sheets in agreement with SWAXS experiments, which show that the lamellar structure is recovered on cooling down. LCTEM images showed that the smallest nanostructures are dark and contain iron, while the biggest ones are white and could be tentatively assigned to CO_2 and/or H_2 bubbles (**Figure 12**).

The difference in size of nanostructures between those observed by TEM at high temperature on powders and those observed by liquid TEM and AFM and in temperature DLS measurements on reaction mixture suggested that both dioctylether solvent and oleic acid in the reaction mixture should contribute to stabilizing smaller nanostructures when the temperature increases. Oleic acid is an amphiphilic molecule suitable to generate “reverse” vesicles in the organic solvent. The melting of lamellar iron stearate compounds in the reaction mixture should be associated with their stabilization by oleic acid in dioctylether. Oleic acid would interact around melted iron stearates and should also contribute to decreasing the size of droplet-like nanostructures. The formation of such metallic-based reverse vesicles in the organic solvent has been poorly reported.^[53]

At a higher temperature than 200 °C, TEM on FeSt_2 powder shows that droplet-like particles are always present and mainly amorphous, but a molecular crystallization is observed above 200 °C at the beginning of the nucleation (200–280 °C). Nuclei appear clearly in the globular particles from 280 °C at the already reported nucleation temperature. Lassenberger^[16] also observed also by SAXS a diffracting structure before the nucleation takes place. We may notice that the observed molecular crystallization occurs simultaneously with the appearance of a white halo (purely organic, no Fe atoms are present), which surrounds the droplet-like particles above 200 °C. We know that during the nucleation step, there is a departure of two stearate chains and simultaneously Fe(III) cations are reduced in Fe(II) . Both phenomena occur in the temperature range of 200–300 °C. Therefore, one may attribute the white halo to the released stearate chains around nanostructures (**Figure 11**). The molecular crystallization is really observed from 230–250 °C and interplanar distances corresponding to interlamellar distances different from those observed in native iron stearates (suggesting a partial interdigitation of stearate chains) are noticed. Further works are still needed to identify the crystalline molecular phase, which is formed before the nucleation.

Nuclei are observed within nanostructure when powders were heated at higher temperatures. In the reaction mixture,

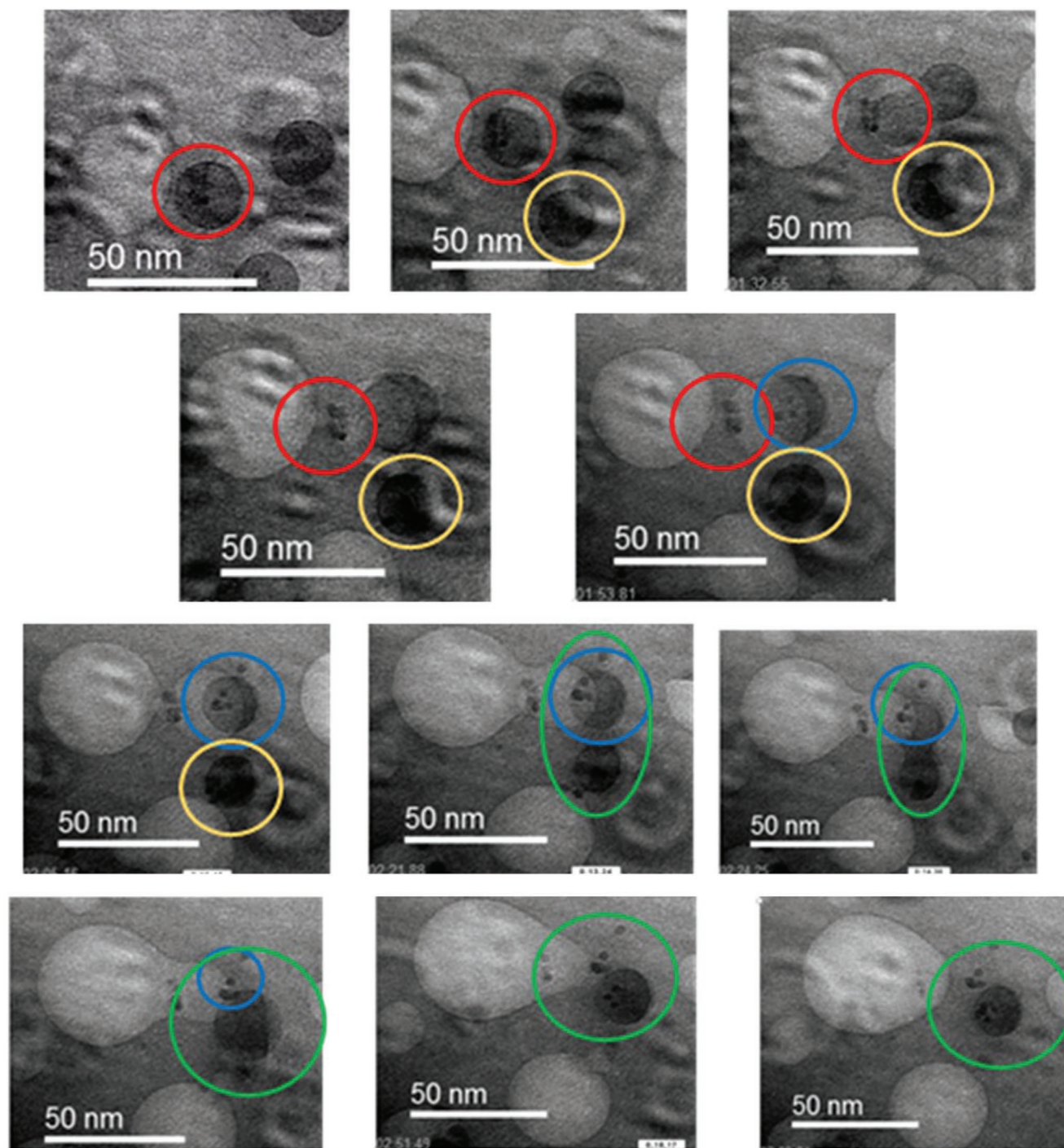


Figure 10. In situ liquid cell TEM images as a function of irradiation time. Red circles: formation of nuclei inside droplet-like nanostructures and then ejection of nuclei from these nanostructures; yellow and blue circles: nuclei form inside nanostructures which “redissolve”; blue circles: merging/coalescence of two nanostructures leading to nucleation and further nuclei ejection.

LC-TEM allowed evidencing that the nucleation occurs in dark/iron-rich vesicles. As soon as the nuclei are formed, they are then ejected outside the nanostructures/nanoreactors (Figure 11 and video), but the nanostructure remains stable.

We have also performed a standard IONPs synthesis experiment up to 280 °C and then observed the reaction mixture by

TEM. As shown in Figure S24, Supporting Information, such droplet-like nanostructures were identified, confirming that this confined nucleation occurs also in standard conditions.

As metals are well-known to form self-assembled lamellar structures in the presence of long-chain carboxylic acids, this mechanism involving confined nanoreactors should be

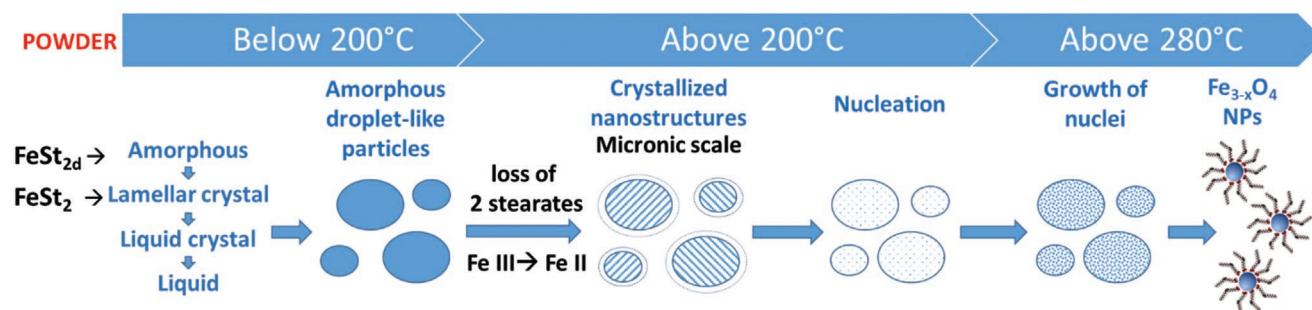


Figure 11. Scheme of the events with the iron stearate powders heated from room temperature up to IONPs formation. The steps above 200 °C have been obtained from high-temperature TEM experiments.

relatively general for most metal oxides NPs obtained via thermal decomposition in an organic solvent in the presence of complexing surfactants, such as long-chain organic acids. Indeed, we have also observed the formation of such nanostructures during the synthesis of manganese oxide NPs (Figure S25, Supporting Information). In addition, such a new confined nucleation mechanism in an organic solvent in nanoreactors composed of long carboxylate chains coordinated to iron polynuclear complexes would explain the high difficulties in obtaining IONPs doped homogeneously by other metal cations.^[54–57] Indeed, the doping elements should need to be integrated into the nanoreactors. Such nanostructures would also explain why IONPs formed easily at the surface of carbon materials, such as carbon nanotubes or few-layer graphene:^[58–60] the alkyl chains at the periphery of the nanoreactors should favor their anchoring at the surface of carbon materials.

4. Conclusion

We have investigated the thermal behavior of two iron stearates used as iron precursors in the TD process by using different techniques, such as SWAXS, SAXS, liquid AFM, liquid cell TEM, and in situ TEM at high temperature. All experiments performed on powders and preheated reaction media evidenced for the first time the formation of droplet-like particles resulting from the melting of iron stearate particles during the temperature increase. The reaction mixture containing long-chain carboxylic acid (oleic acid) and dioctylether led to smaller droplet-like nanostructures due to temperature and surfactant stabilization effects. Then, when the iron stearates

begin to lose stearate chains in the nucleation temperature range, a molecular crystallization of these nanostructures is observed. Further studies will aim at characterizing this crystalline phase. Finally, nucleation occurs within these droplet-like nanostructures, acting as nanoreactors and when nuclei are formed and stable, they are ejected from these nanostructures suggesting that the growth occurs outside these nanostructures. This nucleation confined in nanostructures in organic media explains why the nucleation and growth steps are well separated in the TD process. The observed behavior can be described as a Lamer process-driven via precursors confinement. Such a mechanism of confined nucleation is demonstrated for the first time thanks to a combination of fine in situ characterization techniques and paves the way towards a better mastering of structural NPs parameters. As most metals form self-assembled lamellar structures in the presence of long-chain organic acids, this nucleation mechanism in confined nanoreactors should be relatively general for many NPs of divalent and trivalent metal oxides obtained via thermal decomposition in an organic solvent in the presence of complexing surfactants, such as long-chain organic acids.

5. Experimental Section

Synthesis of Both Iron Stearate Precursors: Iron stearate (II) named FeSt₂ was prepared following a previously reported protocol^[12] (detailed in Supporting Information) by precipitation of sodium stearate and ferrous chloride salt in an aqueous solution. FeSt₂ is a lamellar compound with the composition [Fe₃(μ₃-O)St₆·xH₂O]Cl and mainly Fe III cations.

Heat treatment on FeSt₂ was performed in an oven at 140 °C for 48 h and the resulting compound was named FeSt_{2d}. Its structure

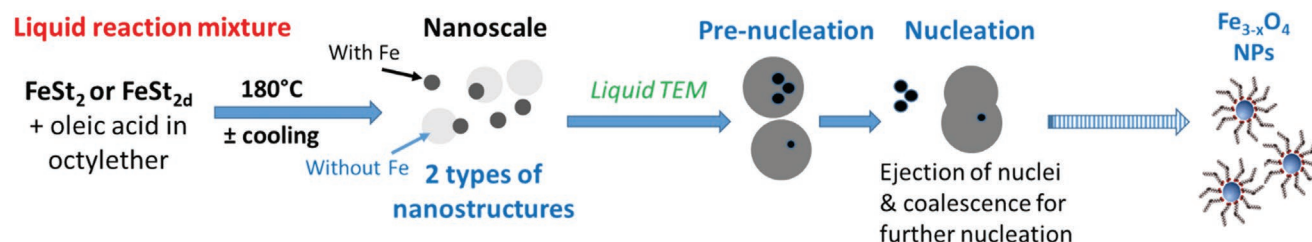


Figure 12. Characterization of the liquid reaction mixture after the homogenization step at 120 °C by different techniques: 1) Evidence of the presence of two types of droplet-like nanostructures: FeSt₂: AFM: 53 ± 6 and 74 ± 7 nm and TEM observations. FeSt_{2d}: AFM: 17.5 ± 4 and 37 ± 6 nm, Liquid cell TEM: 30–50 nm and 15 nm, DLS in T: when T > 60 °C, size distribution decreases, (white droplet-like nanostructures correspond to gas bubble, whereas dark droplet-like nanostructures consist of iron stearates) and 2) schematic evolution of the liquid reaction mixtures in LCTEM leading to iron oxide NPs.



Figure 13. Left: schematic representation of the experimental protocol used for the preparation of LC-TEM experiments. First, 2.2 mmol in iron of iron stearate were mixed with 4.4 mmol of oleic acid in 20 mL octylether used as a solvent. The mixture was stirred and heated at 120 °C for 60 min without a reflux condenser in order to dissolve the reactants and remove the water residues. 1) One droplet of the previously heated solution was deposited over the bottom chip. 2 and 3) The top chip was placed rapidly over to avoid drying taking care of the proper alignment of the windows. 4) The lid was placed to close the system, fix both chips in position with the screws assuring the proper tightness to avoid any leaking to the TEM column. Right: scheme of the LC-TEM set-up and experiments. The thickness between the two SiN membranes is 150 nm.

and composition are detailed in Supporting Information. FeSt_{2d} is amorphous and displays two main polynuclear complexes (polycations) (Figure S4, Supporting Information): $[\text{Fe}_3(\mu_3\text{-O})\text{St}_6\cdot x\text{H}_2\text{O}]\text{St}$ and another one with higher Fe content ($[\text{Fe}_7(\mu_3\text{-O}(\text{H}))_6(\mu_2\text{-O}(\text{H})),_x\text{St}_{12-x}]\text{St}$),^[12,13] and with only Fe III cations.^[44]

Synthesis Conditions of Iron Oxide NPs with a Mean Size of 10 nm: IONPs were synthesized from an already reported reproducible protocol^[10] which consisted of TD of the synthesized iron stearate in the presence of OA (99%, Alfa Aesar) in OE (99%, Sigma). The as-synthesized iron stearate (1.38 g for FeSt_2 and FeSt_{2d} , 2.2 mmol in iron) was mixed with OA (1.24 g, 4.4 mmol) in 20 mL of OE in a two neck RBF. The mixture was stirred and heated at 120 °C for 1 h without a reflux condenser in order to dissolve the reactants and remove the volatile molecule residues. It was demonstrated earlier that if the heating step at 120 °C was suppressed, the mean size was smaller.^[22] The hypothesis was that such volatile molecule residues, and in particular, water, would affect the thermal stability of the iron complex.

Preparation of “Reaction Mixture”: Characterizations were conducted on samples consisting of “reaction mixtures” after this mixing step at 120 °C (and a cooling down or just/directly after the treatment at 120 °C).

Synthesis of IONPs: After the previous mixing step at 120 °C, the cooler was then connected to the flask, and the solution was heated to boiling temperature (≈ 290 °C) with a heating rate of 5 °C min^{-1} and heated to reflux for 2 h under air. After cooling to RT, a black suspension was obtained, which was solubilized in 10 mL of chloroform. The NPs were then precipitated by the addition of an excess of acetone the first time and washed three times with chloroform and acetone at a ratio of 1:4 at 14 000 rpm for 5 min by centrifugation. The NPs were finally suspended in 50 mL of THF.

The NPs synthesized using either FeSt_2 or FeSt_{2d} display a mean diameter of 10.3 ± 0.8 and 10.2 ± 0.9 , respectively (Figure S1a,b, Supporting Information). IONPs were also synthesized by decomposing only FeSt_2 (without solvent and oleic acid) and slightly oxidized magnetite NPs, with a mean size of 11.9 ± 2.3 nm, and a rather spherical shape was obtained (Figure S1c, Supporting Information).

Differential Scanning Calorimetry: DSC measurements were performed with a TA Instruments DSCQ1000 instrument operated at a scanning rate of 5 °C min^{-1} on heating and on cooling.

SWAXS: SWAXS measurements were performed with a transmission Guinier-like geometry. A linear focalized monochromatic Cu $K_{\alpha 1}$ beam ($\lambda = 1.5405$ Å) was obtained using a sealed-tube generator (600 W) equipped with a bent quartz monochromator. The samples were filled in homemade sealed cells of 1 mm path. The sample temperature was controlled within ± 0.01 °C, and exposure times were varied from 2 to 24 h. The patterns were recorded with a curved Inel CPS120 counter gas-filled detector and on image plates scanned by STORM 820 from Molecular Dynamics with 50 μm resolution.

SAXS: SAXS measurements were performed at the Institut Charles Sadron (ICS), CNRS-UPR 22, France, with Rigaku diffractometer

operating with a microfocus rotating anode generator (Micromax-007 HF, 40 kV 30 mA, Cu K_{α} radiation, $\lambda = 1.54$ Å). The X-ray beam was monochromatized and focused with Confocal Max-Flux Optics (Osmic) fitted with a three-pinhole collimation system. The beamstop was equipped with a PIN diode to determine the transmission factor. In the SAXS configuration, the intensity was collected with a 2D multiwire camera located at 0.81 m from the sample and covering a scattering vector range of $0.011 \text{ Å}^{-1} < q < 0.33 \text{ Å}^{-1}$ (q is defined as $4\pi/\lambda \sin[\theta/2]$, where θ is the scattering angle). Samples were introduced between thin calibrated mica cells (1 mm apart), and sample temperature was controlled within ± 0.05 °C. The intensities were corrected according to usual procedures. Data were radially integrated, corrected for electronic background, detector efficiency, empty cell scattering, thicknesses, and transmission factors. Fluorescence contribution from iron content was recorded from FeCl_3 solution and removed from sample measurements. Scattering from pure solvent was recorded for subtraction from sample measurements.

In Situ TEM at High Specimen Temperature: The stearate samples were deposited onto amorphous carbon grids (thickness 30 nm) and observed by imaging and electron energy-loss spectroscopy (EELS) in an electron microscope. In situ high-temperature treatment was realized either by continuous heating in a high-temperature specimen stage or by pulsed heating with infrared laser pulses. An ultrafast TEM that allows exposing the samples to laser pulses (7 ns, 1064 nm) was used for these experiments. The combination of continuous with pulsed heating allowed us to compare equilibrium with non-equilibrium dynamics and to obtain an upper limit of the timescale for the TD of stearates.

In Situ Liquid Cell TEM: LC-TEM is a method, which allows to study the liquid specimens.^[28] Inside the TEM, a high vacuum should be generally present and because of this, only solid samples can be analyzed in the traditional modes, as the liquid samples are incompatible with a vacuum environment.^[61]

The development of the LC-TEM (Figure 13) was possible due to the significant progress in the fabrication of new windows that are electron transparent, thin enough for allowing reasonable imaging, and with a controlled submicrometer separation between the windows where the liquid should be confined. The liquid cell was made of a thin layer of silicon nitride (30–50 nm), which was deposited onto a silicon wafer. The silicon was etched from the back to form a window with dimensions around 100 μm to allow the beam to pass. The wafer was diced into chips that were placed face to face with a spacer material in between like in a sandwich.^[28]

The liquid cell for the TEM was made of two microchips placed together like in a sandwich. All the preparation needs to be done in a place with low dust. Carbon-coated tweezers were used to take the microchips from the storage box and then placed in a beaker with acetone for 2 min to remove the coated polymers from the surface of the microchips, which protect the membrane. The microchips were transferred from the beaker with acetone and placed for 2 min in ethanol and another 2 min in ultrapure ethanol to eliminate completely all the

residues. The microchips were removed from the beaker with ethanol and dried using a thin flow of compressed air. All those manipulations were realized carefully to avoid the damage to the cell. The microchips were placed for 5 s at Plasma Cleaner to make the surface of the silicon nitride membrane hydrophilic. A light microscope was used to check that membrane does not indicate any rupture or fragility.

AFM: AFM images were performed under organic solvents (dioctylether, octadecene) using a Bioscope Resolve instrument (Bruker Nano, Palaiseau, France). Silicon wafers were first sonicated in an acetone/ethanol (1:1) bath for 10 min and dried under nitrogen flow. After this procedure, silicon wafers were cleaned for 30 min with UV–Ozone Cleaner (Novascan) and then coated with polydopamine by immersion for 15 min in a solution of dopamine at 4 g L^{-1} in 10 mM TRIS buffer (pH 8). Substrates were extensively rinsed with milli-Q water and then dried under nitrogen flow. 100 μL of NP suspension was deposited 10 min onto the substrate and then rinsed with the appropriate solvent before imaging. Topographical images were performed by Peakforce TappingTM mode. Silicon nitride cantilevers of conical shape purchased from Bruker (PeakForce Tapping HIRS-FA, Bruker nano, Palaiseau, France) with a spring constant of about 0.35 N m^{-1} were used for both imaging and mechanical measurements. All images were recorded with a resolution of 256×256 pixels and a scan rate of 1 Hz. Sections and size distribution were obtained with the nanoscope analysis software.

Supporting Information

Supporting Information is available from the Wiley Online Library or from the author.

Acknowledgements

The Region Alsace, France, and the Labex Chimie des Systemes Complexes, University of Strasbourg, France are gratefully acknowledged for the doctoral fellowship to Geoffrey Cotin. This research project was also co-funded by Labex CSC, Alsace contre le cancer, INCA (project PRTK14, THERAMAG 2014–225), the French national agency for research (ANR) under the project InSiChem ANR-16-CE05-0011, and EQUIPEX program of the Agence Nationale de Recherche (France), contract ANR-11-EQPX-0041 (project UTEM). The authors thank Mr. Guillaume Fleith for realizing the SAXS measurements at the Institut Charles Sadron (ICS), CNRS-UPR 22, France. C.S. thanks the University of Strasbourg Institut of Advanced Study. The authors acknowledge the Spectroscopy and Microscopy Service Facility (SMI) of LCPME (Université de Lorraine-CNRS—<http://www.lcpme.cnrs-nancy.fr>) for AFM analyses.

Conflict of Interest

The authors declare no conflict of interest.

Data Availability Statement

The data that support the findings of this study are available in the supplementary material of this article.

Keywords

iron oxide nanoparticles, iron stearate, nucleation mechanisms, thermal decomposition, vesicle-like nanoreactors

Received: January 19, 2022

Revised: March 6, 2022

Published online: April 15, 2022

- [1] J. Park, K. An, Y. Hwang, J.-G. Park, H.-J. Noh, J.-Y. Kim, J.-H. Park, N.-M. Hwang, T. Hyeon, *Nat. Mater.* **2004**, *3*, 891.
- [2] T. Hyeon, S. S. Lee, J. Park, Y. Chung, H. B. Na, J. *Am. Chem. Soc.* **2001**, *123*, 12798.
- [3] S. Sun, H. Zeng, D. B. Robinson, S. Raoux, P. M. Rice, S. X. Wang, G. Li, *J. Am. Chem. Soc.* **2004**, *126*, 273.
- [4] S. G. Kwon, Y. Piao, J. Park, S. Angappane, Y. Jo, N.-M. Hwang, J.-G. Park, T. Hyeon, *J. Am. Chem. Soc.* **2007**, *129*, 12571.
- [5] M. V. Kovalenko, M. I. Bodnarchuk, R. T. Lechner, G. Hesser, F. Schäffler, W. Heiss, *J. Am. Chem. Soc.* **2007**, *129*, 6352.
- [6] G. Cotin, C. Kiefer, F. Pertont, D. Ihiwakrim, C. Blanco-Andujar, S. Moldovan, C. Lefevre, O. Ersen, B. Pichon, D. Mertz, S. Bégin-Colin, *Nanomaterials* **2018**, *8*, 881.
- [7] B. P. Pichon, O. Gerber, C. Lefevre, I. Florea, S. Fleutot, W. Baaziz, M. Pauly, M. Ohlmann, C. Ulhaq, O. Ersen, V. Pierron-Bohnes, P. Panissod, M. Drillon, S. Bégin-Colin, *Chem. Mater.* **2011**, *23*, 2886.
- [8] A. Walter, C. Billotey, A. Garofalo, C. Ulhaq-Bouillet, C. Lefevre, J. Taleb, S. Laurent, L. V. Elst, R. N. Muller, L. Lartigue, F. Gazeau, D. Felder-Flesch, S. Bégin-Colin, *Chem. Mater.* **2014**, *26*, 5252.
- [9] V. K. LaMer, R. H. Dinegar, *J. Am. Chem. Soc.* **1950**, *72*, 4847.
- [10] W. Baaziz, B. P. Pichon, S. Fleutot, Y. Liu, C. Lefevre, J.-M. Grenèche, M. Toumi, T. Mhiri, S. Bégin-Colin, *J. Phys. Chem. C* **2014**, *118*, 3795.
- [11] Y. Xia, Y. Xiong, B. Lim, S. E. Skrabalak, *Angew. Chem. Int. Ed.* **2009**, *48*, 60.
- [12] G. Cotin, C. Kiefer, F. Pertont, M. Boero, B. Özdamar, A. Bouzid, G. Ori, C. Massobrio, D. Bégin, B. Pichon, D. Mertz, S. Bégin-Colin, *ACS Appl. Nano Mater.* **2018**, *1*, 4306.
- [13] G. Cotin, F. Pertont, C. Petit, S. Sall, C. Kiefer, V. Bégin, B. Pichon, C. Lefevre, D. Mertz, J.-M. Grenèche, S. Bégin-Colin, *Chem. Mater.* **2020**, *32*, 9245.
- [14] L. M. Bronstein, X. Huang, J. Retrum, A. Schmucker, M. Pink, B. D. Stein, B. Dragnea, *Chem. Mater.* **2007**, *19*, 3624.
- [15] B. H. Kim, K. Shin, S. G. Kwon, Y. Jang, H.-S. Lee, H. Lee, S. W. Jun, J. Lee, S. Y. Han, Y.-H. Yim, D.-H. Kim, T. Hyeon, *J. Am. Chem. Soc.* **2013**, *135*, 2407.
- [16] A. Lassenberger, T. A. Grünwald, P. D. J. van Oostrum, H. Rennerhofer, H. Amenitsch, R. Zirbs, H. C. Lichtenegger, E. Reimhult, *Chem. Mater.* **2017**, *29*, 4511.
- [17] F. Pertont, G. Cotin, C. Kiefer, J.-M. Strub, S. Cianferani, J.-M. Grenèche, N. Parizel, B. Heinrich, B. Pichon, D. Mertz, S. Bégin-Colin, *Inorg. Chem.* **2021**, *60*, 12445.
- [18] H. F. Drake, G. S. Day, S. W. Vali, Z. Xiao, S. Banerjee, J. Li, E. A. Joseph, J. E. Kuszynski, Z. T. Perry, A. Kirchon, O. K. Ozdemir, P. A. Lindahl, H.-C. Zhou, *Chem. Commun.* **2019**, *55*, 12769.
- [19] P. N. Nelson, R. A. Taylor, *Appl. Petrochem. Res.* **2014**, *4*, 253.
- [20] A. Skoulios, D. Guillon, *Mol. Cryst. Liq. Cryst. Inc. Nonlinear Opt.* **1988**, *165*, 317.
- [21] H. Abied, D. Guillon, A. Skoulios, P. Weber, A. M. Giroud-godquin, J. C. Marchon, *Liq. Cryst.* **1987**, *2*, 269.
- [22] A. M. Giroud-Godquin, J. C. Marchon, D. Guillon, A. Skoulios, *J. Phys. Chem.* **1986**, *90*, 5502.
- [23] P. Maldivi, D. Guillon, A.-M. Giroud-Godquin, J.-C. Marchon, H. Abied, H. Dexpert, A. Skoulios, *J. Chim. Phys.* **1989**, *86*, 1651.
- [24] S. Pu, C. Gong, A. W. Robertson, *R. Soc. Open sci.* **2020**, *7*, 191204.
- [25] A. S. Kashin, V. P. Ananikov, *Nat. Rev. Chem.* **2019**, *3*, 624.
- [26] J. J. De Yoreo, N. A. J. M. Sommerdijk, *Nat. Rev. Mater.* **2016**, *1*, 16035.
- [27] N. de Jonge, F. M. Ross, *Nat. Nanotechnol.* **2011**, *6*, 695.
- [28] *Liquid Cell Electron Microscopy*, (Ed: F. M. Ross), Cambridge University Press, Cambridge **2016**.
- [29] N. O. Peña, D. Ihiwakrim, M. Han, B. Lassalle-Kaiser, S. Carenco, C. Sanchez, C. Laberty-Robert, D. Portehault, O. Ersen, *ACS Nano* **2019**, *13*, 11372.
- [30] J. J. D. Yoreo, *Prog. Cryst. Growth Charact. Mater.* **2016**, *62*, 69.

- [31] N. T. K. Thanh, N. Maclean, S. Mahiddine, *Chem. Rev.* **2014**, *114*, 7610.
- [32] T. J. Woehl, J. E. Evans, I. Arslan, W. D. Ristenpart, N. D. Browning, *ACS Nano* **2012**, *6*, 8599.
- [33] K. L. Jungjohann, S. Bliznakov, P. W. Sutter, E. A. Stach, E. A. Sutter, *Nano Lett.* **2013**, *13*, 2964.
- [34] J. Baumgartner, A. Dey, P. H. H. Bomans, C. Le Coadou, P. Fratzl, N. A. J. M. Sommerdijk, D. Faivre, *Nat. Mater.* **2013**, *12*, 310.
- [35] U. Mirsaidov, J. P. Patterson, H. Zheng, *MRS Bull.* **2020**, *45*, 704.
- [36] Y. Zhang, D. Keller, M. D. Rossell, R. Erni, *Chem. Mater.* **2017**, *29*, 10518.
- [37] T. J. Woehl, T. Moser, J. E. Evans, F. M. Ross, *MRS Bull.* **2020**, *45*, 746.
- [38] N. M. Schneider, M. M. Norton, B. J. Mendel, J. M. Grogan, F. M. Ross, H. H. Bau, *J. Phys. Chem. C* **2014**, *118*, 22373.
- [39] T. J. Woehl, P. Abellan, *J. Microsc.* **2017**, *265*, 135.
- [40] N. Bhattachai, D. L. Woodall, J. E. Boercker, J. G. Tischler, T. H. Brintlinger, *Nanoscale* **2019**, *11*, 14573.
- [41] J. Cookman, V. Hamilton, L. S. Price, S. R. Hall, U. Bangert, *Nanoscale* **2020**, *12*, 4636.
- [42] C. de Gracia Lux, B. Donnio, B. Heinrich, M. P. Krafft, *Langmuir* **2013**, *29*, 5325.
- [43] E. B. Sirota, H. E. King, D. M. Singer, H. H. Shao, *J. Chem. Phys.* **1993**, *98*, 5809.
- [44] F. Pertion, *Ph.D. report*, University of Strasbourg, **2019**.
- [45] H. Chang, B. H. Kim, H. Y. Jeong, J. H. Moon, M. Park, K. Shin, S. I. Chae, J. Lee, T. Kang, B. K. Choi, J. Yang, M. S. Bootharaju, H. Song, S. H. An, K. M. Park, J. Y. Oh, H. Lee, M. S. Kim, J. Park, T. Hyeon, *J. Am. Chem. Soc.* **2019**, *141*, 7037.
- [46] A. Feld, A. Weimer, A. Kornowski, N. Winckelmans, J.-P. Merkl, H. Kloust, R. Zierold, C. Schmidtke, T. Schotten, M. Riedner, S. Bals, H. Weller, *ACS Nano* **2019**, *13*, 152.
- [47] K. Morigaki, P. Walde, *Langmuir* **2002**, *18*, 10509.
- [48] M. Delample, F. Jérôme, J. Barrault, J.-P. Douliez, *Green Chem* **2011**, *13*, 64.
- [49] S.-H. Tung, H.-Y. Lee, S. R. Raghavan, *J. Am. Chem. Soc.* **2008**, *130*, 8813.
- [50] J. M. Grogan, N. M. Schneider, F. M. Ross, H. H. Bau, *Nano Lett.* **2014**, *14*, 359.
- [51] F. Kiss, J. Teplý, *Int. J. Radiat. Phys. Chem.* **1971**, *3*, 503.
- [52] K.-S. Kim, J.-M. Lee, H.-Y. Seo, J.-H. Kim, H.-P. Song, M.-W. Byun, J.-H. Kwon, *Radiat. Phys. Chem.* **2004**, *71*, 47.
- [53] S. K. P. Velu, M. Yan, K.-P. Tseng, K.-T. Wong, D. M. Bassani, P. Terech, *Macromolecules* **2013**, *46*, 1591.
- [54] W. Baaziz, B. P. Pichon, Y. Liu, J.-M. Grenèche, C. Ulhaq-Bouillet, E. Terrier, N. Bergeard, V. Halté, C. Boeglin, F. Choueikani, M. Toumi, T. Mhiri, S. Begin-Colin, *Chem. Mater.* **2014**, *26*, 5063.
- [55] L. E. De-León-Prado, D. A. Cortés-Hernández, J. M. Almanza-Robles, J. C. Escobedo-Bocardo, J. Sánchez, P. Y. Reyes-Rdz, R. A. Jasso-Terán, G. F. Hurtado-López, *J. Magn. Magn. Mater.* **2017**, *427*, 230.
- [56] D. Peddis, N. Yaacoub, M. Ferretti, A. Martinelli, G. Piccaluga, A. Musinu, C. Cannas, G. Navarra, J. M. Greneche, D. Fiorani, *J. Phys.: Condens. Matter* **2011**, *23*, 426004.
- [57] A. E. Deatsch, B. A. Evans, *J. Magn. Magn. Mater.* **2014**, *354*, 163.
- [58] W. Baaziz, L. Truong-Phuoc, C. Duong-Viet, G. Melinte, I. Janowska, V. Papaefthimiou, O. Ersen, S. Zafeiratos, D. Begin, S. Begin-Colin, C. Pham-Huu, *J. Mater. Chem. A* **2014**, *2*, 2690.
- [59] X. Liu, I. Marangon, G. Melinte, C. Wilhelm, C. Ménard-Moyon, B. P. Pichon, O. Ersen, K. Aubertin, W. Baaziz, C. Pham-Huu, S. Bégin-Colin, A. Bianco, F. Gazeau, D. Bégin, *ACS Nano* **2014**, *8*, 11290.
- [60] G. Melinte, I. Florea, S. Moldovan, I. Janowska, W. Baaziz, R. Arenal, A. Wisnet, C. Scheu, S. Begin-Colin, D. Begin, C. Pham-Huu, O. Ersen, *Nat. Commun.* **2014**, *5*, 4109.
- [61] F. M. Ross, *Science* **2015**, *350*, aaa9886.